JGR Space Physics

RESEARCH ARTICLE
10.1029/2024JA032525

Key Points:

- We present the variability in Martian atomic hydrogen brightness from early Martian year (MY) 36 to the first quarter of MY 37
- Martian exospheric H Ly-β and γ emissions reach their peak brightness during the southern summer of MY 36
- Martian corona is much brighter at H Ly-β wavelength in MY 37 compared to the previous year due to increased solar irradiance

Correspondence to:
R. Susarla,
raghuramsusarla@gmail.com;
susarla.raghuram@lasp.colorado.edu

Citation:
Susarla, R., Deighan, J., Chaffin, M. S., Jain, S., Lillis, R. J., Chirakkil, K., et al. (2024). Variability of atomic hydrogen brightness in the Martian exosphere: Insights from the emirates ultraviolet spectrometer on board emirates Mars mission. *Journal of Geophysical Research: Space Physics*, *129*, e2024JA032525. https://doi.org/10.1029/2024JA032525

Received 5 FEB 2024
Accepted 9 JUN 2024
Corrected 29 JUN 2024

This article was corrected on 29 JUN 2024. See the end of the full text for details.

Author Contributions:
Conceptualization: R. Susarla
Formal analysis: R. Susarla
Investigation: R. Susarla, J. Deighan
Methodology: R. Susarla
Project administration: J. Deighan
Software: R. Susarla
Supervision: J. Deighan, M. S. Chaffin, S. Jain
Validation: R. Susarla
Visualization: S. Jain
Writing – original draft: R. Susarla
Writing – review & editing: R. Susarla, M. S. Chaffin

Variability of Atomic Hydrogen Brightness in the Martian Exosphere: Insights From the Emirates Ultraviolet Spectrometer on Board Emirates Mars Mission

R. Susarla[1,2], **J. Deighan**[1], **M. S. Chaffin**[1], **S. Jain**[1], **R. J. Lillis**[3], **K. Chirakkil**[1,2], **D. Brain**[1], **E. Thiemann**[1], **F. Eparvier**[1], **F. Lootah**[4], **G. Holsclaw**[1], **M. Gacesa**[5], **M. O. Fillingim**[3], **N. El-Kork**[2,5], **S. England**[6], **J. S. Evans**[7], **H. AlMazmi**[8], and **H. AlMatroushi**[4]

[1]Laboratory for Atmospheric and Space Physics, University of Colorado Boulder, Boulder, CO, USA, [2]Space & Planetary Sciences Group, Khalifa University, Abu Dhabi, UAE, [3]Space Sciences Laboratory, University of California, Berkeley, CA, USA, [4]Mohammed Bin Rashid Space Centre, Dubai, UAE, [5]Physics Department, Khalifa University, Abu Dhabi, UAE, [6]Department of Aerospace and Ocean Engineering, Virginia Polytechnic Institute and State University, Blacksburg, VA, USA, [7]Computational Physics Inc. Springfield, Springfield, VA, USA, [8]United Arab Emirates Space Agency, Abu Dhabi, UAE

Abstract

The Emirates Mars Ultraviolet Spectrometer (EMUS), aboard the Emirates Mars Mission (EMM), has been conducting observations of ultraviolet emissions within the Martian exosphere. Taking advantage of the distinctive orbit of the EMM around Mars, EMUS utilizes a dedicated strafe observation strategy to scan the illuminated Martian exosphere at tangential altitudes ranging from 130 to over 20,000 km. To distinguish between emissions of Martian origin and those from the interplanetary background, EMUS conducts specialized background observations by looking away from the planet. This approach has allowed us to investigate the radial and seasonal variations in Martian coronal emission features at H Lyman-α, β and γ wavelengths. Our analysis supports the previous studies indicating that Martian exospheric hydrogen Lyman emission brightness attains its highest levels around the southern summer solstice and reaches its lowest levels when Mars is near aphelion. Additionally, a secondary peak emission at all altitudes is observed after perihelion during Martian Year (MY) 36, which can be attributed to a Class C dust storm. Our study establishes a strong correlation between solar flux and coronal brightness for these emissions, highlighting the impact of solar activity on the visibility of Martian corona. In addition, we have examined interannual variability and found that emission intensities in MY 37 surpassed those in MY 36, primarily due to increased solar activity. These observations help to understand potential seasonal patterns of exospheric hydrogen, which is driven by underlying mechanisms in the lower atmosphere and solar activity, eventually suggesting an impact on water loss in the Martian atmosphere.

Plain Language Summary

Atomic hydrogen primarily forms as a product when Martian water undergoes various photochemical reactions. These hydrogen atoms encircle Mars and become illuminated by solar radiation, leading to the creation of Martian hydrogen corona. The Emirates Mars Ultraviolet Spectrometer (EMUS), on the Emirates Mars Mission spacecraft, is currently studying the Martian atmosphere using the ultraviolet light emissions of different atoms and molecules on Mars. In this study, we have analyzed EMUS observations and determined that atomic hydrogen emission intensities increase during the Martian southern summer and decrease as Mars moves farther away from the Sun. Furthermore, we have compared the hydrogen brightness between two consecutive Martian years and have found that the hydrogen brightness is higher in the most recent year primarily due to increased solar radiation. These observations help us understand possible patterns that occur during different seasons on Mars and the mechanisms underlying water loss in the Martian atmosphere.

1. Introduction

Perpetual observations of the Martian atmosphere are essential for a comprehensive understanding of the escape of water from the surface of Mars into space. These observations must be coupled with modeling work to decipher Mars' responses to varying solar radiation across different seasons. Earlier models propose the gradual transport of water to the Martian upper atmosphere, where it undergoes photodissociation, leading to the formation of H_2

after a sequence of chemical reactions (McElroy & Donahue, 1972; Parkinson & Hunten, 1972; Yung et al., 1988). A portion of the transported H_2 gives rise to hydrogen atoms through reactions with $O(^1D)$ and CO_2^+, as well as through photodissociation (Hunten & McElroy, 1970). The scale height of atomic hydrogen is larger than that of any other Martian species due to its lower mass, making hydrogen the predominant element in the Martian exosphere, extending to several tens of Martian radii (D. E. Anderson & Hord, 1971; Feldman et al., 2011; Chaffin et al., 2015). A substantial fraction of hydrogen atoms remains bound to Mars in satellite orbits, while other atoms successfully surmount the gravitational barrier, escaping into space. This establishes a persistent mechanism for the loss of water on Mars.

Solar radiation dissociates CO_2 into CO and O, but the direct recombination of these species is a slow process that does not suffice to sustain the long-term presence of CO_2 in the Martian atmosphere (Atreya & Blamont, 1990). Earlier modeling efforts have highlighted the pivotal role of water in stabilizing the Martian CO_2 atmosphere through odd-hydrogen chemistry (Atreya & Blamont, 1990; Atreya & Gu, 1995; McElroy, 1972; McElroy & Donahue, 1972; McElroy et al., 1976; Nair et al., 1994; Parkinson & Hunten, 1972). The oxidation of CO is achievable through heterogeneous chemistry, where interactions with species such as H_2O_2, OH, O, and O_2 take place, and their formation is associated with H_2O. These reactions ultimately lead to the recycling of CO_2 (Atreya & Blamont, 1990; Atreya & Gu, 1994, 1995). Therefore, the study of the present evolving nature of Martian water loss holds immense significance in understanding the past and future aspects of Martian climate, geological evolution, and its potential to support life (Jakosky, 2021).

As explained before, water is the ultimate source of atomic hydrogen in the Martian atmosphere. Therefore, understanding water loss from the Martian environment relies heavily on the observations of atomic hydrogen. Solar photons at Lyman wavelengths induce fluorescence in both the populations of Martian-bound and escaping hydrogen atoms through resonance fluorescence excitation, illuminating the Martian hydrogen corona (D. E. Anderson & Hord, 1971, 1977). Due to the combination of intense solar radiation and the high resonance efficiency of atomic hydrogen at a wavelength of 121.6 nm, H I Lyman-α emerges as the most prominent emission feature in the observed far-ultraviolet spectra of Mars (Barth, 1969). The investigation of these hydrogen spectroscopic emissions enables us to gain insights into the global distribution of atomic hydrogen and its variations across seasons. This, in turn, aids in addressing the loss rate of H_2O from the Martian atmosphere.

The scattered emissions of atomic hydrogen at the Lyman-α wavelength have been extensively investigated using various spacecrafts, including ultraviolet spectrometers onboard Mariner 6, 7, and 9 (D. E. Anderson & Hord, 1971; J. Anderson Donald, 1974), Mars 2, 3, and 5 (Babichenko et al., 1977; Dostovalov & Chuvakhin, 1973), the Spectroscopy for the Investigation of the Characteristics of the Atmosphere of Mars (SPICAM) instrument on board Mars Express (MEX) (Chaffin et al., 2014; Chaufray et al., 2008) and the Imaging Ultraviolet Spectrograph (IUVS) onboard Mars Atmosphere and Volatile Evolution mission (MAVEN) (Chaffin et al., 2018; Clarke et al., 2017; Mayyasi et al., 2018; McClintock et al., 2015). The remote observations from space-borne telescopes such as the Hubble Space Telescope (HST) (Bhattacharyya et al., 2015; Clarke et al., 2014), the Hopkins Ultraviolet Telescope (HUT) Telescope Feldman et al. (2002), the Far Ultraviolet Spectroscopic Explorer (FUSE) (Krasnopolsky & Feldman, 2002), the Rosetta spacecraft (Feldman et al., 2011), and the Hisaki Space telescope (Masunaga et al., 2020, 2022) have also significantly contributed to the understanding of long-term seasonal and short term variabilities of Martian atmosphere. These remote observations targeted the Martian atmosphere across different seasons and covered altitudes ranging from 80 km to several tens of Martian radii. Several other measurements of atomic hydrogen have also been conducted using the Analyzer of Space Plasma and Energetic Atoms (ASPERA-3) on board MEX (Futaana et al., 2006; Gunell et al., 2006) and the Solar Wind Ion Analyzer (SWIA) and Neutral Gas and Ion Mass Spectrometer (NGIMS) on board the Mars Atmosphere and Volatile Evolution (MAVEN) spacecraft (Halekas et al., 2015; Stone et al., 2020). Further observations from these instruments and the subsequent analysis of the collected data have been carried out in multiple studies (Bhattacharyya, Clarke, Chaufray, et al., 2017; Bhattacharyya et al., 2015; Bhattacharyya et al., 2020; Chaffin et al., 2018; Chaufray, Gonzalez-Galindo et al., 2021; Chaufray, Mayyasi, et al., 2021; Halekas, 2017; Halekas et al., 2015, 2017; Rahmati et al., 2018).

Previous models had supported the notion that atomic hydrogen escapes the Martian atmosphere at a slow and consistent rate (Barth, 1974). However, long-term observations conducted by missions such MEX, MAVEN, and HST have revealed that the rate of hydrogen loss varies significantly, ranging from one to several orders of magnitude during the southern summer compared to periods near perihelion (Bhattacharyya et al., 2015; Chaffin et al., 2014; Clarke et al., 2014). But the recent multi-instrument data analysis by Chaffin et al. (2021) has demonstrated that regional dust events can amplify the rate of hydrogen escape by 5–10 times. Similarly, the recent upper atmosphere observations by JAXA's Hisaki space telescope, in conjunction with data from several other instruments, have shown that during a major dust storm in Martian year (MY) 33, the abundance of hydrogen in the upper atmosphere gradually increases, leading to higher escape rates (Masunaga et al., 2022). These studies conclude that seasonal or impulsive variations in dust activity can transport water directly to higher altitudes, resulting in an enhancement of the hydrogen escape rate.

All the experiments discussed previously have provided observations of atomic hydrogen with limited spatial and temporal coverage of Mars. A comprehensive study of the transient behavior of water vapor in the Martian atmosphere, originating from the surface and influenced by solar radiation and photochemistry in the lower atmosphere, necessitates continuous observations from a high-altitude orbit. To achieve this objective, the Emirates Mars Mission (EMM) launched the "Hope" probe equipped with a suite of three advanced remote sensing scientific instruments: the Emirates eXploration Imager (EXI), the Emirates Mars InfraRed Spectrometer (EMIRS), and the Emirates Mars Ultraviolet Spectrometer (EMUS) on 20 July 2020 (Almatroushi et al., 2021). EMM was placed in a unique Mars orbit with a period of approximately 55 hr, enabling nearly-continuous observations of the Martian surface to exosphere at different seasons through the combined observations of three instruments. EMUS, a photon-counting imaging spectrograph, is dedicated to capturing emissions from key constituents of the Martian atmosphere, scanning the thermosphere (100–200 km) to the exosphere (above 200 km), in the wavelength range of 100–170 nm with the observed spectral range gradually increasing from the edge of the field of view to the center at 83–180 nm due to the circular active region of the detector. For a detailed description of the instrument's design and observation modes refer to Holsclaw et al. (2021).

In this study, we present an analysis of EMUS/EMM observations of the daylit Martian exosphere and interplanetary background. The aim of our current research is to examine variability of dayside atomic hydrogen brightness across different seasons from early Martian year 36 to the first quarter of Martian year 37. It extends the findings of ongoing and prior investigations by conducting a thorough examination of temporal changes in atomic hydrogen under the influence of increased solar activity.

2. Description of EMUS Atomic Hydrogen Observations and Data Analysis

The unique science orbit of the EMM around Mars, ranging from approximately 20,000 km at periapsis to about 43,000 km at apoapsis, offers significant advantages for achieving nearly complete global coverage of Mars with a diurnal coverage period of approximately 10 days (Amiri et al., 2022). This distinctive orbit enabled the EMUS/EMM instrument to scan Martian atmospheric emissions of key species from altitudes of approximately 130 km up to several Martian radii (>6 R_M) over the course of more than one Martian year. This extent of coverage in both time and space exceeds the capabilities of previous missions. More insights of the instrument design, key objectives and observation strategies aimed at studying the Martian atmosphere are described by Holsclaw et al. (2021).

EMUS/EMM has been conducting observations of Mars using various observation strategies to comprehend the three-dimensional global variations in the atmosphere. To systematically scan across the foreground daylit Martian exosphere, the strafe observation strategy U-OS4a, in which EMUS view directions are across the orbit plane and perpendicular to the Mars-Sun line, has been employed while scanning the tangential altitudes above 130 km up to as high as 12 Mars Radii (see the top left and bottom panels of Figure 1). These observations are intended to scan the Martian exosphere, achieving a spatial resolution of ≤300 km for altitudes between 1.06 and 1.60 R_M, and ≤1,000 km for altitudes between 1.6 and 6.0 R_M. The observations occurred with a mean temporal frequency of approximately four per orbit (Holsclaw et al., 2021).

The U-OS4b observations are designed to investigate background emission intensities, enabling us to distinguish between hydrogen emissions originating from Mars and those from emitted by hydrogen originating elsewhere throughout the broader solar system. In this observation scenario, EMUS/EMM measures the brightness of interplanetary background emission by looking in the same direction as that of foreground but on the opposite side of the spacecraft orbit, and away from the Mars system (see top right panel of Figure 1). The mean temporal frequency for these observations is similar to that of U-OS4a.

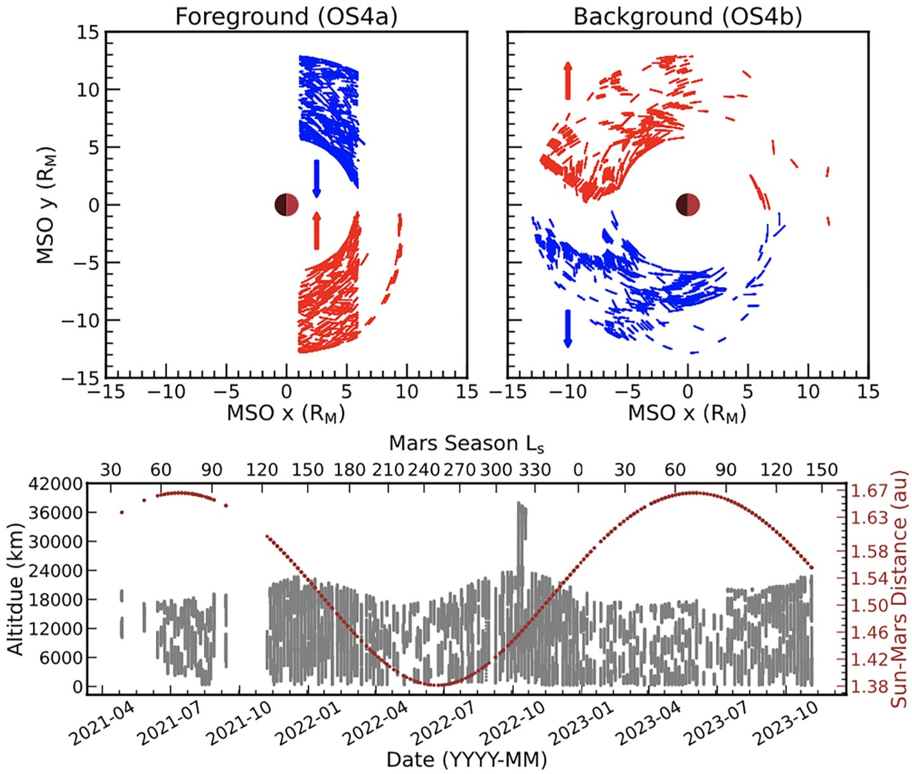

Figure 1. Observation geometry: EMUS/EMM locations during foreground cross-exosphere (top left) and background interplanetary observations (top right). Blue and red arrows represent the EMUS/EMM instrument look direction along MSO −Y and +Y directions, respectively. In top panels the sun is located on the right side of the figure. The bottom panel shows EMUS' scanning altitude coverage during foreground cross-exosphere observations, with Sun-Mars distance plotted on the right *y*-axis.

The trajectories of EMM around Mars, depicted in the Mars-centric Solar Orbital (MSO) frame, and the observational direction of the EMUS during the foreground (U-OS4a) and background (U-OS4b) observation strategies are illustrated in Figure 1. The MSO frame comprises a +X axis that points from Mars to the Sun. The inertially referenced velocity of the Sun relative to Mars is the secondary vector, and the +Y axis represents the component of this velocity vector orthogonal to the +X axis. The +Z axis completes the right-handed system In U-OS4a mode, EMUS/EMM is capable of scanning the Martian exosphere, covering tangent point altitudes ranging from 130 km above the Martian surface to altitudes exceeding 20,000 km. Particularly noteworthy is that during Mars' traversal of solar longitudes (Ls) between 317° and 323°, EMUS/EMM extends its observational reach to higher altitudes over 36,000 km (see the bottom panel of Figure 1). A data gap between 2021 and 09–13 and 2021-11-06 occurred due to solar conjunction. During U-OS4b observations, EMUS/EMM observes interplanetary emission intensities at spacecraft altitudes spanning from 5.8 Mars radii (R_M) up to 13 R_M, all while looking away from Mars.

Each U-OS4 observation is mostly aligned with either MSO +Y or −Y look directions, corresponding to dusk or dawn direction, depending on the spacecraft location for both foreground and background observations. Figure 2 illustrates the sky coverage for both these look directions in foreground and background observation strategies. In the background observations, EMUS/EMM surveys the sky across a range of ±40° of declination (DEC) for all right ascension angles (RA), utilizing a swath of approximately 10° along the slit length, which has similar coverage for the foreground observations. This figure also emphasizes the temporal progression of EMUS observations with repeated background sky coverage (see yellow shaded region in this figure). This repeated sky coverage helps us to understand the variability of background emission intensity measured at different seasons of the Mars.

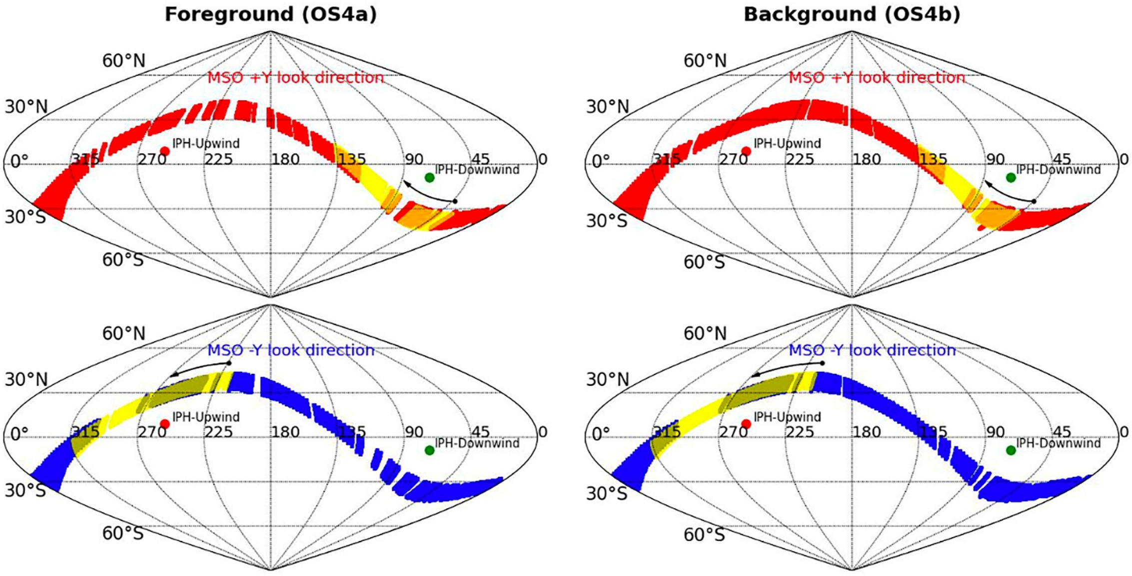

Figure 2. Sky coverage maps of EMUS in foreground and background observation modes plotted in Ecliptic J2000 coordinates. The top and bottom panels depict sky coverage in MSO +Y and −Y look directions, respectively. Curved arrows indicate the sky coverage direction over time, and yellow shaded regions indicate repeated observed regions in the sky coverage since the beginning of observations. Red and green dots represent the interplanetary hydrogen upwind and downwind bulk flow directions, respectively.

To investigate the hydrogen variability in the daylit Martian exosphere, we have utilized the Level 2a version 4.0 data sets of U-OS4a and U-OS4b observations in this analysis, which are publicly available at sdc.emiratesmarsmission.ae. This data set covers a substantial observation period, starting from 25 April 2021, and extending through 21 August 2023, encompassing more than one Martian year. Specifically, it spans from early MY 36 (Ls = 37°) and extends well into the first quarter of MY 37 (Ls = 110°). An example EMUS spectra for both foreground and background observations are presented in Figure 3. In all these observed spectra, we detect the first three emission lines of the ultraviolet Lyman series atomic hydrogen, Ly-α, Ly-β, and Ly-γ, simultaneously. By integrating suitable radiative transfer models for the prevailing solar conditions, the simultaneous

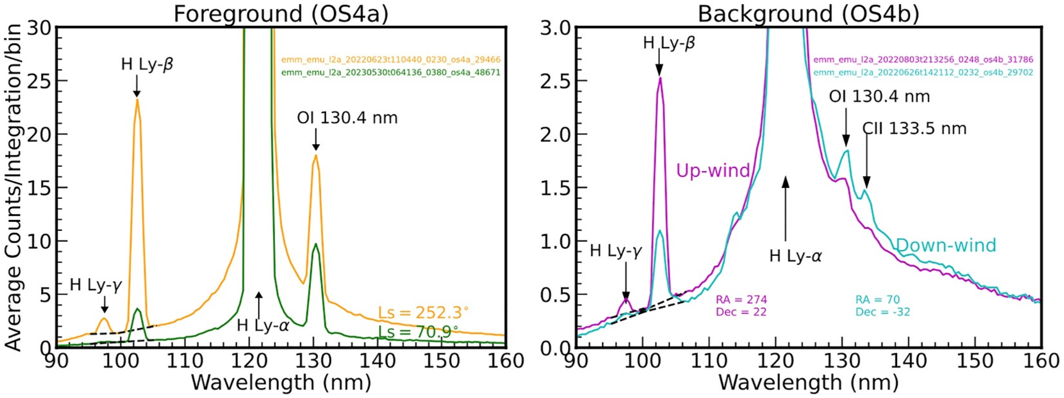

Figure 3. The averaged observed detector count spectra for foreground (left panel) and background (right panel) observation scenarios along the spatial and integration dimensions. The coronal spectra in foreground are co-added in the tangential altitudes range between 2500 and 4,000 km for both aphelion (Ls = 252.3°) perihelion (Ls = 70.9°) periods. The interplanetary hydrogen upwind and downwind spectra in the right panel are recorded for RA = 274°, DEC = 22°, and RA = 70°, DEC = −32° locations, respectively in Ecliptic J2000. Salient Martian and Interplanetary background atomic emission features are indicated with vertical arrows at their corresponding wavelengths. The black dashed curves under the H Ly-β and γ emission features represent the background H Ly-α emission intensity. The detector exposure time is 42 and 60 min for upwind and downwind background spectra, respectively, while foreground spectra they are 24 and 19 min for perihelion and aphelion periods.

detection of these lines in the Martian exosphere helps to explore the interaction of solar photons with hydrogen within the Martian exosphere. Meanwhile, the emission lines in the background spectra can provide insights into the radiative properties of hydrogen in the interplanetary medium at these wavelengths.

In all the EMUS/EMM observations, the spread of H Lyman-α photons across a wide wavelength range is influenced by both the emission's brightness and the broad wings of the instrument line spread function. As a result, these photons contribute as underlying signals to the features of H Lyman-β, γ, and other emissions. To mitigate the impact of H Lyman-α emission intensity on these other features, we apply a wing-subtraction technique to each observed spectrum. For both H Lyman-β and γ emission features, we calculate the average radiance on the red and blue sides of the emission line and subtract this average from the core of the emission line.

In these observation modes, stars occasionally appear in the instrument's field of view, generating intense signal features that are limited to a few spatial bins. To minimize the influence of these background signals, we have developed an algorithm capable of detecting spatial bins associated with high-intensity emission features produced by stars. For the given integration, we average the observed counts along the wavelength dimension, excluding the H-Ly-α wavelength region. When stars enter in the field of view of the instrument during the observation, the resulting mean signal along the spatial pixel dimension exhibits strong peaks indicative of their presence. Leveraging the capabilities of `scipy.signal`, specifically the `find_peaks` class, we identify all peaks in the mean count spectrum across spatial bins and calculate their prominences. To refine our peak identification, we compute the mean prominences on the left and right sides of the initially identified peaks using the scipy library. Subsequently, we further enhance the precision of the identified peaks by applying an additional constraint. Peaks are refined based on the mean prominence, and spatial bins with intense signal counts are singled out with a relative height constraint of 0.5. In scenarios where the signal attributable to stars is relatively small compared to the background, this procedure may not successfully identify those star locations. In this case, the peaks associated with stars may not exhibit significant prominence compared to the overall signal, and as a result, they might go undetected. However, it's important to note that these undetected star locations typically do not exert any significant impact on our calculations. The procedure primarily focuses on identifying spatial pixels with prominent and distinct peaks, which are indicative of regions where stars contribute substantially to the observed signal. Spatial pixels associated with stars exhibit high prominence and are consequently excluded from the analysis in both U-OS4a and U-OS4b observations.

After the wing-subtraction and the removal of spatial bins associated with stars, we integrate the radiance beneath the emission feature to calculate the total emission intensity in Rayleigh units (1 Rayleigh is equivalent to $10^6/(4\pi)$ photons sec^{-1} cm^{-2} ster^{-1}). Two example counts spectra, which are averaged across spatial and integration dimensions, obtained for both foreground and background observations are showcased in Figure 3. A substantial difference in the observed counts is evident during cross-exospheric observations when Mars is positioned near perihelion ($\text{Ls} = 252°$) and aphelion ($\text{Ls} = 71°$). Similarly, distinct variability in the measured counts is also observable when the instrument is oriented along the directions of interplanetary hydrogen bulk flow, whether upwind or downwind. In addition to the atomic hydrogen Lyman emissions, variations in the atomic oxygen emission feature at 130.4 nm are discernible in this figure. Further exploration of the spatial and temporal variability of atomic emissions in these oxygen observations is discussed in a separate study (Chirakkil et al., 2024). The emission feature near 133.5 nm is due to singly ionized carbon atom, which has importance in studying the elemental abundance of dust components in the Interstellar medium (Slavin, 2009).

Following wing subtraction and star removal procedures for the U-OS4a data set, the observed signal for coronal H Lyman emissions still represents a combination of emissions from the Martian exosphere and the interplanetary background. The interplanetary background hydrogen emission intensities vary depending on the instrument's line of sight across the celestial sphere. We provide a more detailed explanation of the background subtraction method employed for the U-OS4a coronal emission intensities in Section 4.

Unfortunately, a continuous decline in the sensitivity of the EMUS micro-channel plate detector occurred at the location of the bright Ly-α signal, resulting in a reduction in the observed H Ly-α emission radiance. This decrease in instrument sensitivity is particularly pronounced in observations made after January 2022 ($\text{Ls} > 152°$, MY 36), and its effect is negligible before this period. Consequently, in this analysis, we have considered the calculated H Ly-α emission intensities from the beginning of the mission until just before this degradation period for both foreground and background observations.

To investigate the effect of variation in solar radiation on Martial exosphere throughout the EMUS observation period, we used solar irradiance data from the Extreme Ultraviolet Monitor (EUVM) aboard the MAVEN mission (Eparvier et al., 2015; Thiemann et al., 2017). The EUVM instrument on MAVEN consists of three broadband radiometers that measure solar irradiance using specific filters: Channel A covers wavelengths of 0.1–3 nm and 17–22 nm, Channel B covers wavelengths of 0.1–7 nm, and Channel C covers wavelengths of 121–122 nm. These broadband irradiance measurements from the MAVEN EUV monitor are used in a Flare Irradiance Spectral Model (FISM)-Mars to generate the complete EUV spectrum at Mars ranging from 0 to 190 nm, with daily and minute averages. Additional information about the EUVM instrument design and FISM-M model is available in Eparvier et al. (2015) and Thiemann et al. (2017), respectively.

3. Interpretation of EMUS Interplanetary Hydrogen Background Observations

As mentioned earlier, the EMUS background observations cover various locations across the Martian sky at different times. These observations measure the emission intensities of the IPH by scanning the Martian sky along the MSO +Y and −Y look directions. When the instrument faces the upwind flow of the IPH, it records higher emission intensities of H Lyman emissions compared to when it faces downwind locations. For each observation, we calculated the phase angle between the instrument's look direction and the bulk flow direction of the IPH, as shown in the bottom panel of Figure 4. It is evident that at different times, aligning the instrument along MSO ±Y look directions results in observations of the IPH in upwind (angles close to 0°), downwind (angles closer to 180°), and cross-wind (angles closer to 90°) directions. The top three panels of Figure 4 illustrate variations in observed background hydrogen radiances at H Lyman α, β, and γ wavelengths for both MSO +Y and −Y look directions across different seasons of Mars. It can be noticed that the observed H Lyman emission intensities distinctly vary when the instrument is directed toward IPH upwind and downwind directions during different observation times, whereas the emission intensities remain consistent for the cross-wind look directions.

Prior to the reduced detector sensitivity period, periodic variations in background H Ly-α brightness are evident, primarily originating from solar rotation (see third panel of Figure 4). We also plotted the normalized EUVM solar fluxes in the third panel on the right y-axis which show period variation due to solar rotation. We noticed a phase shift of about 13–15 days between the H Ly-α brightness for EMUS' MSO +Y and −Y look directions, which is corresponding to nearly half of the solar rotation period (Bertaux et al., 1999; Quémerais et al., 2006). This is mainly due to the instrument covering the Martian sky with a difference of about 180° in right ascension angle along MSO +Y and −Y look directions. This results in the coverage of nearly opposite sides of the Martian sky for consecutive observations. As the Sun rotates, these brighter illuminated background regions of sky come into the field of view of the instrument for the corresponding look directions at different times.

Between March 2022 and October 2022, we observe an increase in H Ly-β and γ emission intensities for both MSO +Y and −Y look directions. Notably, the change in intensity is more pronounced in the MSO +Y look direction than in the latter (refer to Figure 4). During this period, Mars traverses the region between Ls 180 and 360° in MY 36. This systematic change in intensities can be linked to an additional component from the higher density of hydrogen of Martian origin, driven by Mars's proximity to the Sun during this specific period. Our calculated phase angle between EMUS/EMM look direction and the interplanetary hydrogen (IPH) bulk flow direction in Figure 4 indicates that EMUS' MSO +Y looks toward the IPH upwind, while -Y looks toward the downwind, during the Mars perihelion passage period. IPH emission intensities are naturally higher in the upwind direction compared to the downwind direction (Baliukin et al., 2022; Lallement, Bertaux, & Dalaudier, 1985; Lallement, Bertaux, & Kurt, 1985; Möbius et al., 2004; Vallerga et al., 2004; Witte, 2004). The observed background brightnesses are influenced by the seasonal variation of the Martian exosphere and add to the observed brightness. Thus, during this period, for MSO +Y look direction which is aligned with the IPH upwind, has a significant increase in the H Lyman emission brightness compared to the MSO −Y look direction.

When Mars is receding farther from the Sun in MY 37, despite EMUS looking toward IPH upwind and downwind directions, no increment in H Lyman emissions is noticed. Moreover, the IPH brightnesses for H Lyman β and γ emissions remain similar when comparing the repeated sky coverage areas during Mars' passage through the aphelion periods in MY 36 and 37 (Compare the shaded region with initial period of observations in Figure 4). This also supports that Mars exospheric emission intensities significantly contribute during Mars perihelion passage compared to aphelion seasons. The observed background emission intensities, which are conducted at spacecraft altitudes ranging from 20,000 km to 45,000 km, are driven by both interplanetary hydrogen and

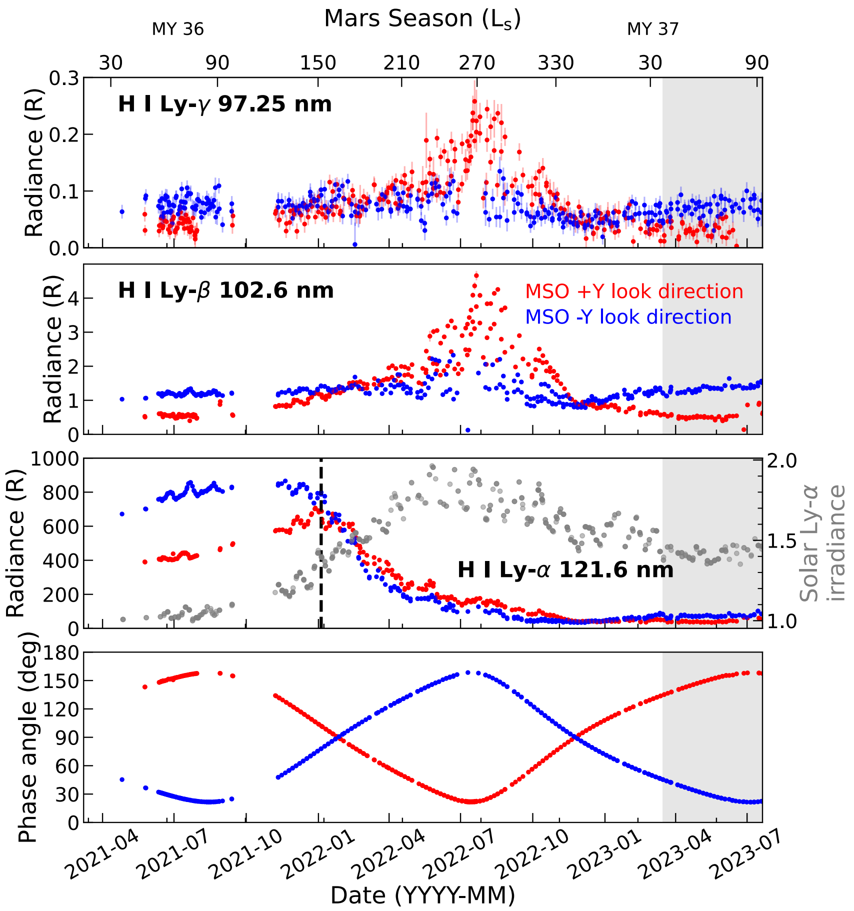

Figure 4. Variability of EMUS observed background H Lyman emission intensities: Temporal changes in Hydrogen Lyman emissions during the U-OS4b background observation scenario are depicted in the top three panels. The bottom panel illustrates the phase angle between the EMUS look direction and the interplanetary hydrogen bulk flow upwind directions. The shaded region indicates the repeated segment of the sky coverage since the initiation of the observation. A vertical dashed line on the third panel indicates the commencement of reduced detector sensitivity period for H Ly-α. Error bars, depicted with a one-σ standard mean in the sample, are too small to be noticeable in H Ly-β and α emissions. The normalized EUVM solar H Ly-α fluxes are plotted on the right y-axis of third panel which are showing periodic variations due to rotation of the Sun.

Martian exospheric emissions. When Mars is situated farther away from the Sun, the exospheric hydrogen column densities at these higher altitudes tend to be quite low, and the contribution from hydrogen of Martian origin to the background observations is relatively minor. Thus, the observed background intensities during the Mars' aphelion passage are mostly contributed by interplanetary hydrogen and remained almost constant. However, caution should be exercised as the solar flux at the H Lyman wavelengths also undergoes changes during this observation period, which could potentially influence the observed radiance contributed by both the exosphere and interplanetary hydrogen.

Though the sensitivity of detector around 121 nm is diminished, we were able to see an increase in H Ly-α brightness for MSO + Y look direction relative to -Y look direction (see Figure 4), which is similar to H Ly-β, when Mars is traversing Ls between 180 and 360°. It is difficult to notice these distinct features for different MSO look directions in case of H Ly-γ because the background emission intensities are much smaller compared to Ly-β and α.

We also ruled out the possibility of atomic oxygen in the observed background H Ly β emission intensity. Atomic oxygen can scatter solar radiation at wavelengths close to 102.7 nm, primarily due to its allowed electronic transition levels (Meier et al., 1987). On the disk of the planet interpretation of the brightness at 102.7 nm is complicated by solar resonant fluorescence from an atomic oxygen multiplet. However, a recent comprehensive

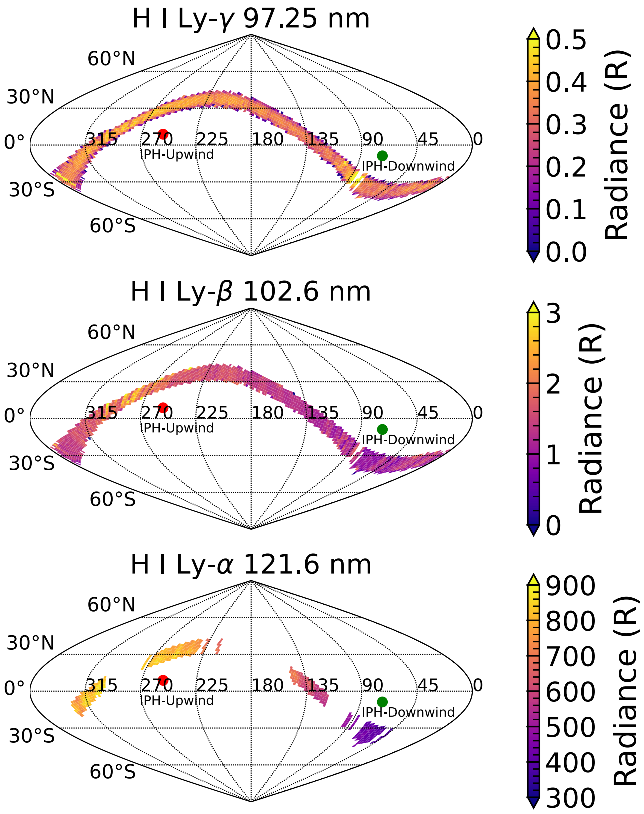

Figure 5. Sky maps of mean interplanetary atomic hydrogen Lyman emission intensities observed in the U-OS4b scenario. The emission intensities are plotted in Ecliptic J2000 coordinates. The red and green circles represent the IPH upwind and downwind flow directions, respectively. Gaps in the H Ly-*α* sky map result from the decline in the detector sensitivity as explained in the main text.

analysis of hydrogen and oxygen emissions at 102.6 nm by Chaffin et al. (2021) suggests that above 500 km altitudes, the contributions from atomic oxygen are negligible. Consequently, the observed seasonal variation in H Ly-*β* predominantly reflects the variability of hydrogen rather than the involvement of atomic oxygen. This is supported by the fact that above 500 km, the hot oxygen component, which is bound to Mars, is significantly smaller by several orders of magnitude and rapidly decreases with increasing altitude (Chaffin et al., 2021; Chirakkil et al., 2024; Deighan et al., 2015). However, the background observations of EMUS are done above 20,000 km tangential altitude, where the role of atomic oxygen can safely be neglected.

Figure 5 displays sky maps illustrating the observed mean emission intensities of IPH emissions in the Ecliptic J2000 frame. A notable trend of decreasing IPH brightness as the right ascension angle increases is observed for all H Lyman emission lines. It can be noticed in H Ly-*α* and Ly-*β* emission maps that the emission intensities reach their maximum values in the IPH upwind direction and are at their minimum near the downwind flow direction, which is consistent with earlier IPH observations (Baliukin et al., 2022). As explained before, the gaps observed in the sky maps for H Ly-*α* emission are a result of the limited amount of data considered in this analysis before the loss in instrument sensitivity.

4. Interpretation of EMUS Foreground Martian Daylit Coronal Observations

Our comprehensive analysis of both foreground and background observation data sets has enabled us to investigate the seasonal variation of hydrogen in the Mars exosphere region. This was accomplished by subtracting background emission intensities from the foreground observations. In each specific foreground observation, we utilized the nearest in time background sky emission intensity for the background subtraction process separately for both MSO +Y and −Y look directions. The mean seasonal variation of coronal H Lyman emission intensity profiles at different Sun-Mars distance bins is presented in Figure 6 for tangent point altitudes above 500 km. As anticipated, the intensity profiles of observed Lyman coronal emissions vary as a function of the Sun-Mars distance, with maximum intensity occurring when Mars is closer to the Sun and minimum intensity when it is farther away. This figure illustrates that EMUS can effectively study the seasonal variation of these emission intensities at altitudes exceeding 5 R_M. We could not study the H Ly-*α* emission variability beyond Ls = 153°, MY36 due to the decrease in the instrument's sensitivity at this wavelength. However, the observed H Ly-*α* emission intensity

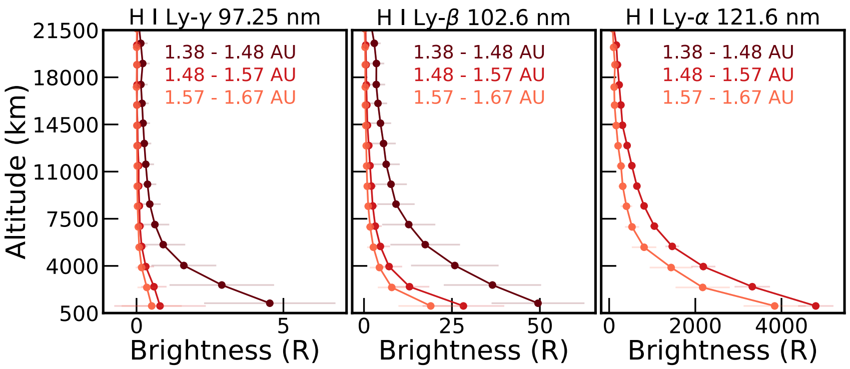

Figure 6. Average emission intensity profiles of H Lyman emissions at different Sun-Mars distance bins. A significant increase in H Ly-*γ* and Ly-*β* emissions can be noticed when Mars is crossing perihelion. Refer to the main text for missing H Ly-*α* emission profile during aphelion period. Error bars represent 1-*σ* standard deviation of the sample.

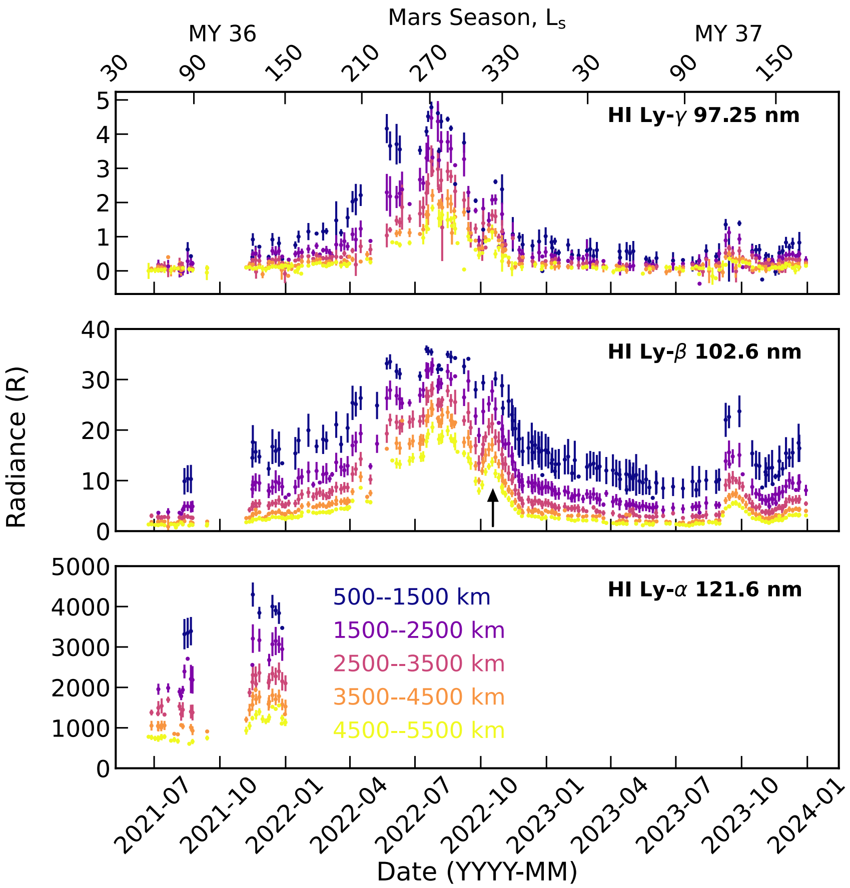

Figure 7. Variability of average emission intensity profiles of H Lyman emissions at different Martian seasons, revealing a substantial increase in H Ly-γ and Ly-β emissions as Mars crosses southern summer solstice. The observed radiances are averaged in 1,000 km bins above 500 km tangential altitude and normalized by the corresponding solar fluxes. Error bars represent 1-σ standard deviation of the sample. Vertical arrow drawn in the middle panel indicates the peak period of class C dust storm.

shows an increase before this solar longitude as Mars moves closer to the Sun. These observations are consistent with earlier measurements of atomic hydrogen variability (Bhattacharyya, Clarke, Chaufray, et al., 2017; Bhattacharyya et al., 2015; Bhattacharyya et al., 2020; Chaffin et al., 2018; Chaffin et al., 2021).

We have illustrated the seasonal variation in H Lyman emission intensities at different tangent point altitude bins above 500 km in Figure 7. To alleviate the influence of solar flux variations in the observations, the observed radiances at a specific wavelength are normalized using the broadband averaged solar irradiance derived from the L3 data product of the EUVM/MAVEN instrument based on the FISM-M model (Thiemann et al., 2017). This normalization involves multiplying the observed radiances by the minimum solar irradiance value and then dividing by the actual solar irradiance corresponding to that wavelength for the EMUS observation period. The highest emission intensities at all altitudes above 500 km occur when Mars is around Ls 270° in MY 36, followed by a subsequent decrease in intensities up to Ls 315° due to the seasonal variation of the atmosphere. A secondary peak in emission intensities can also be observed at Ls 321° in Martian year 36, as depicted in this figure. This time frame corresponds to a class C dust storm, occurring within the Ls range of 310.5°–330.2° and peaking at Ls 315° (Kass et al., 2016; Madeleine et al., 2011; Millour et al., 2018). More details about the characteristics of class C dust storm can be found in Mars Climate Database (https://www-mars.lmd.jussieu.fr; Forget et al., 1999; Olsen et al., 2022). The observed H Lyman β peak emission intensity occurred during the declining phase of the dust storm, mirroring the time delay observed in an earlier annually recurring C-type dust storm during MY 34 (Chaffin et al., 2021). Another peak in the H Lyman β emission during Ls 120, MY 37 is associated with another dust storm as Mars moving away from aphelion.

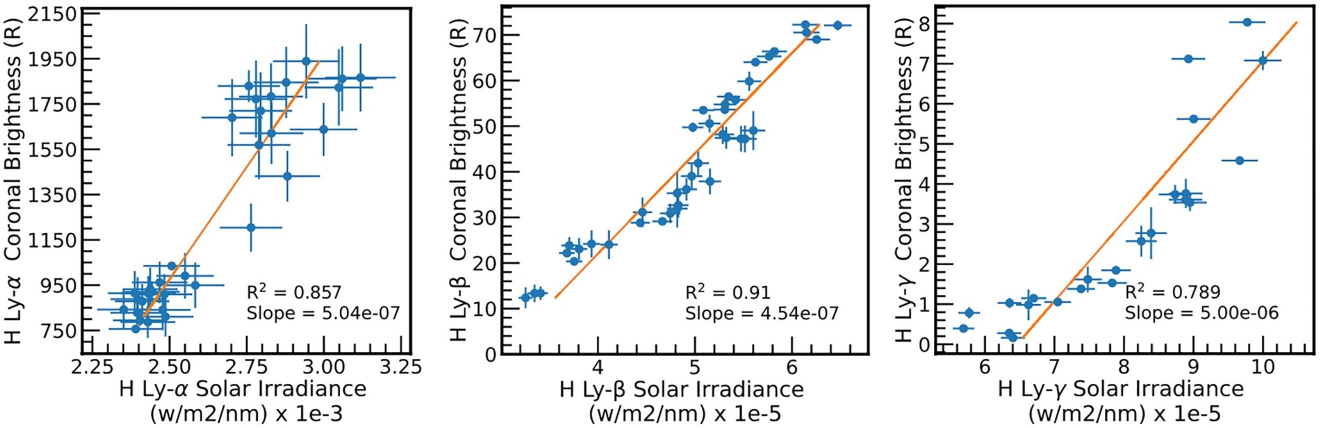

Figure 8. Correlation analysis of Solar Irradiance with Martian coronal H Lyman emission intensities. Horizontal and vertical error bars represents 1-σ standard deviation in the observed radiance and Solar fluxes, respectively.

Previous observations indicate that dust forcing events can enhance H abundances in the exosphere, resulting in higher brightness during such periods (Chaffin et al., 2014, 2021; Clarke et al., 2014; Halekas, 2017; Heavens et al., 2018; Sun et al., 2023). The dust storm peaks around Ls 315° with a secondary peak in emission intensities occurring at Ls 321° with an approximate 10-day gap between the two events. Impulsive dust events in the Martian atmosphere's dynamical system can lift water directly to higher altitudes, leading to greater hydrogen abundances (Chaffin et al., 2021). A photochemical model by Chaffin et al. (2017) demonstrated that the induction of water at high altitudes can produce a large amount of H on a timescale of weeks. This aligns with the observed time gaps between the peak of the dust storm and the occurrence of the peak H emission intensity. We also investigated the impact of variability in solar radiation at Lyman wavelengths during this storm period and did not observe any significant changes in solar radiation at these wavelengths. General circulation models of Mars can assist in studying this behavior to quantitatively assess the increase in hydrogen intensity. However, a more detailed and focused study is needed to comprehensively understand the variability in hydrogen behavior during dust storm periods, which is beyond the scope of the present work.

To study the influence of solar radiation on the Martian exosphere, we conducted a correlation analysis between EUVM onboard MAVEN measured Solar Lyman fluxes and EMUS/EMM observed Martian coronal emission intensities (see Figure 8). A strong positive correlation was observed between the coronal emission intensities and solar fluxes, establishing the fact that Martian coronal intensities increase with increasing solar activity.

A comparison between the emission intensity profiles of H Ly-β for the same Martian seasons was conducted for two different Martian years: MY 36 and MY 37, as illustrated in Figure 9. The emission intensities were averaged over 1,000 km altitude bins for tangential altitudes above 500 km up to 5,500 km. This figure shows that the observed emission intensities in MY 37 were higher compared to those at the same seasons of the earlier MY 36. The noticeable rise in H Ly-β brightness is primarily linked to heightened solar activity (refer to Figure 9). Notably, the solar flux at the H Ly-β wavelength increases by approximately 40%–50% in Martian Year (MY) 37, with model uncertainty below 30% (Thiemann et al., 2017), while the observed emission intensities surpass those of MY 36 by a factor of 2 or more at all altitudes. The increased solar activity causes overall heating and expansion of atmosphere which eventually leads higher hydrogen emission intensities (Mayyasi et al., 2018, 2023). The study by Mayyasi et al. (2018) have shown that the observed H Ly-α emission intensities are enhanced during the solar flare event due to increase in the temperature of upper atmosphere. Thus, the increase in the emission intensities during MY 37 can be attributed to both the elevated solar radiation and also due to variation in the hydrogen densities in the Martian exosphere. The intricate interplay between solar radiation, water content, and hydrogen density highlights the complex dynamics influencing the radiative properties of the Martian atmosphere. The estimation of these parameters to the enhanced Hydrogen Lyman intensity is beyond the scope of the present work. As explained before, EMUS/EMM couldn't make observations between Ls 99 and 123° in MY 36 due to solar conjunction, which did not allow us to compare the brightness profiles in this period. Presently, the Sun is advancing through solar cycle 25, and the sunspot number is on the rise. Consequently, it is expected that we will observe even brighter emission profiles as solar activity continues to increase over time.

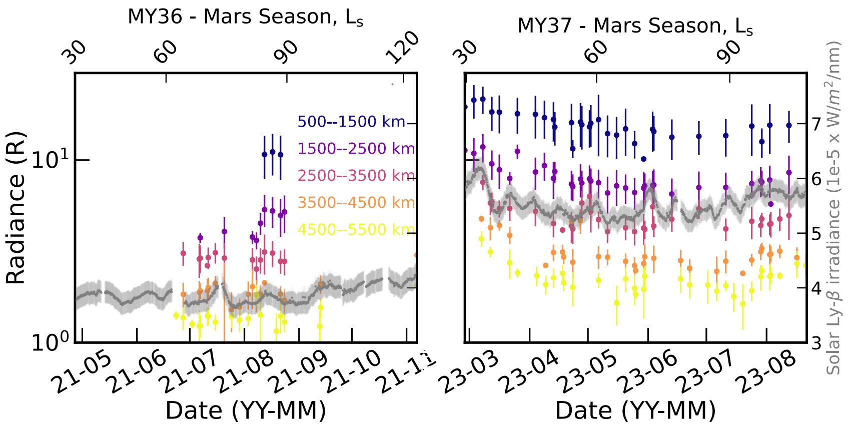

Figure 9. Comparison of H Ly-β emission brightness profiles between Martian years 36 and 37. The observed radiances are averaged in 1,000 km bins above 500 km tangential altitude. Error bars represent 1-σ standard deviation of sample. The data gap between 99 and 123° Ls in MY 36 is due to solar conjunction. The gray curve represents the EVUM/MAVEN observed solar flux for Ly-β wavelength is plotted on the right y-axis of the right panel with 1-σ standard deviation error bars.

5. Summary, Conclusions and Future Prospects

In this study, we examined the variability of H Lyman emission intensities within the sunlit Martian exosphere utilizing the EMUS/EMM strafe observations strategy U-OS4a observations, complemented by data set from U-OS4b mode for more than one Martian year. U-OS4a observations are designed to capture cross-exospheric observations of the sunlit Martian exosphere, while U-OS4b focuses on background emissions from the Martian sky. These distinct observation modes enabled us to differentiate between Hydrogen Lyman emissions originating from interplanetary hydrogen and those from hydrogen bound to Mars.

Utilizing foreground U-OS4a observations, we observed the variability of daylit coronal H Lyman emission brightness, with peak emission intensities occurring during the southern summer period, in line with the expected behavior of seasonal variation on Mars. A secondary emission peak was also noted in the H Lyman emissions at all altitudes during the class C dust storm period. The phase difference between the observed secondary emission peak intensity periods and dust peaks aligns with earlier observations and model predictions. These variations in the H Lyman emission intensities are directly connected to increase hydrogen abundance in the Martian exosphere, which is driven by the solar insolation at Mars and also due to transport of water from lower atmosphere to exosphere directly due to dust storms. The solar activity increased in the recent times which lead higher solar irradiance compared to starting mission phase. Our comparison of brightness profiles across different seasons in two consecutive Martian years also reveals that Martian exosphere responds to the variations in solar irradiance, with the recent year exhibiting a brighter corona compared to the earlier one. These observations suggest that Mars' seasonal response can be unique for a given Martian year, influenced by solar activity and atmospheric conditions.

The sky coverage facilitated by EMUS background observations, which encompass IPH upwind, downwind, and crosswind locations, enabled us to explore IPH emissions across different Martian seasons. Our analysis of the U-OS4b data set revealed a notable contrast in observed IPH brightness between the upwind and downwind locations, consistent with earlier findings summarized by Baliukin et al. (2022). The observed variability in U-OS4b background emission intensity during the southern summer period of Mars represents the intricate interplay between the Martian exosphere and the surrounding interplanetary environment.

Future and ongoing observations of H Lyman emissions hold the potential to provide a more detailed understanding of the individual contributions of the Martian exosphere and interplanetary hydrogen in U-OS4b observations. Taking into account the current level of solar activity, an extensive data analysis and modeling effort aimed at quantifying IPH and exospheric emission intensities for various Martian seasons would enable a comprehensive study. The observed change in H Lyman emission brightness during class C dust storm seasons presents an intriguing phenomenon that warrants further investigation. Utilizing general circulation models coupled with radiation transfer models, we can leverage these observed H Lyman brightness profiles to understand the temperature and density structure of the Martian exosphere across different seasons.

The determination of present-day Martian water loss highly depends on the observed atomic hydrogen brightness profiles at different seasons, a dependence significantly influenced by solar activity. These observed emission profiles undergo fitting with a radiative transfer model to comprehend the thermal distribution of atomic hydrogen in the exosphere and ultimately estimate the water loss rate. Fitting several previously observed Hydrogen Lyman-α brightness profiles invokes a multi-component thermal distribution in the exosphere. This distribution is particularly essential when fitting brightness profiles at higher altitudes (Bhattacharyya, Clarke, Bertaux, et al., 2017; Bhattacharyya, Clarke, Chaufray, et al., 2017; Bhattacharyya et al., 2015; Chaffin et al., 2014; Chaufray et al., 2008; Clarke et al., 2014). Recently, Bhattacharyya et al. (2023) attempted to constrain the hot component of atomic hydrogen by making high altitude observations of Mars, and their model fitting suggests that the Martian water loss rate via non-thermal escape could be as high as 26% of the total thermal escape rate near perihelion and solar minimum conditions. They attributed this higher non-thermal escape rate to solar wind charge exchange at higher altitudes. Similarly, our EMUS-observed high-altitude brightness profiles of atomic hydrogen emission can prove valuable in estimating the contribution of the hot component of hydrogen and subsequently studying escape rates from the Martian exosphere. This approach of will offer valuable insights into the complex interplay of factors affecting the Martian exosphere and its response to external influences and subsequently address the loss rate of Martian water. In conclusion, the observed data set serves as a valuable complement to previous Mars observations, offering crucial insights into current water loss and, consequently, the evolution of the atmosphere.

Data Availability Statement

The EMM/EMUS l2a data we analyze here are available at the EMM Science Data Center (SDC, http://sdc.emiratesmarsmission.ae). This location is designated as the primary repository for all data products produced by the EMM team and is designated as long-term repository as required by the UAE Space Agency. The data available at http://sdc.emiratesmarsmission.ae include ancillary spacecraft data, instrument telemetry, Level 1 (raw instrument data) to Level 3 (derived science products), quicklook products, and data users guides http://sdc.emiratesmarsmission.ae to assist in the analysis of the data. Following the creation of a free login, all EMM data are searchable via parameters such as product file name, solar longitude, acquisition time, sub-spacecraft latitude and longitude, instrument, data product level, and etc. Data products can be browsed within the SDC via a standardized file system structure that follows the convention:/emm/data/<Instrument>/<DataLevel>/<Mode>/<Year>/<Month> Data product filenames follow a standard convention: emm_<Instrument>_<DataLevel>_<StartTimeUTC>_<OrbitNumber>_<Mode>_<Descrip-tion>_<KernelLevel>_<Version>.<FileType> Emirates Mars Ultraviolet Spectrograph (EMUS) data and users guides are available at: http://sdc.emiratesmarsmission.ae. Daily measurements of Solar irradiance L3 data set from EUVM instrument is available at https://pds-ppi.igpp.ucla.edu/data/maven-euv-modelled/.

Acknowledgments
Funding for development of the EMM mission is provided by the UAE government, and to co-authors outside of the UAE by MBRSC. RS and KC are supported by the Grant (8474000332-KU-CU-LASP Space Sci).

References

Almatroushi, H., AlMazmi, H., AlMheiri, N., AlShamsi, M., AlTunaiji, E., Badri, K., et al. (2021). Emirates Mars mission characterization of Mars atmosphere dynamics and processes. *Space Science Reviews*, *217*(8), 89. https://doi.org/10.1007/s11214-021-00851-6

Amiri, H. E. S., Brain, D., Sharaf, O., Withnell, P., McGrath, M., Alloghani, M., et al. (2022). The Emirates Mars mission. *Space Science Reviews*, *218*(1), 4. https://doi.org/10.1007/s11214-021-00868-x

Anderson, D. E., & Hord, C. W. (1971). Mariner 6 and 7 ultraviolet spectrometer experiment: Analysis of hydrogen lyman-α data. *Journal of Geophysical Research*, *76*(28), 6666–6673. https://doi.org/10.1029/JA076i028p06666

Anderson, D. E., & Hord, C. W. (1977). Multidimensional radiative transfer: Applications to planetary coronae. *Planetary and Space Science*, *25*(6), 563–571. https://doi.org/10.1016/0032-0633(77)90063-0

Anderson, J., & Donald, E. (1974). Mariner 6, 7, and 9 ultraviolet spectrometer experiment: Analysis of hydrogen lyman alpha data. *Journal of Geophysical Research*, *79*(10), 1513–1518. https://doi.org/10.1029/JA079i010p01513

Atreya, S. K., & Blamont, J. E. (1990). Stability of the Martian atmosphere: Possible role of heterogeneous chemistry. *Geophysical Research Letters*, *17*(3), 287–290. https://doi.org/10.1029/GL017i003p00287

Atreya, S. K., & Gu, Z. G. (1994). Stability of the Martian atmosphere: Is heterogeneous catalysis essential? *Journal of Geophysical Research*, *99*(E6), 13133–13146. https://doi.org/10.1029/94JE01085

Atreya, S. K., & Gu, Z. G. (1995). Photochemistry and stability of the atmosphere of Mars. *Advances in Space Research*, *16*(6), 57–68. https://doi.org/10.1016/0273-1177(95)00250-I

Babichenko, S. I., Deregusov, E. V., Kurt, V. G., Romanova, N. N., Skliankin, V. A., Smirnov, A. S., et al. (1977). Measurements in interplanetary space and in the Martian upper atmosphere with a hydrogen absorption-cell spectrophotometer for Ly α-radiation onboard Mars 4 - 7 spaceprobes. *Space Science Instrumentation*, *3*, 271–286.

Baliukin, I., Bertaux, J.-L., Bzowski, M., Izmodenov, V., Lallement, R., Provornikova, E., & Quémerais, E. (2022). Backscattered solar Lyman-α emission as a tool for the heliospheric boundary exploration. *Space Science Reviews*, *218*(5), 45. https://doi.org/10.1007/s11214-022-00913-3

Barth, C. A. (1969). Planetary ultraviolet spectroscopy. *Applied Optics*, *8*(7), 1295–1304. https://doi.org/10.1364/AO.8.001295

Barth, C. A. (1974). The atmosphere of Mars. *Annual Review of Earth and Planetary Sciences*, *2*(1), 333–367. https://doi.org/10.1146/annurev.ea.02.050174.002001

Bertaux, J.-L., Kyrölä, E., Quemerais, E., Lallement, R., Schmidt, W., Summanen, T., et al. (1999). Swan observations of the solar wind latitude distribution and its evolution since launch. *Space Science Reviews*, *87*(1/2), 129–132. https://doi.org/10.1023/A:1005178402842

Bhattacharyya, D., Chaufray, J. Y., Mayyasi, M., Clarke, J. T., Stone, S., Yelle, R. V., et al. (2020). Two-dimensional model for the Martian exosphere: Applications to hydrogen and deuterium Lyman α observations. *Icarus*, *339*, 113573. https://doi.org/10.1016/j.icarus.2019.113573

Bhattacharyya, D., Clarke, J. T., Bertaux, J.-L., Chaufray, J.-Y., & Mayyasi, M. (2015). A strong seasonal dependence in the Martian hydrogen exosphere. *Geophysical Research Letters*, *42*(20), 8678–8685. https://doi.org/10.1002/2015GL065804

Bhattacharyya, D., Clarke, J. T., Bertaux, J. L., Chaufray, J. Y., & Mayyasi, M. (2017). Analysis and modeling of remote observations of the Martian hydrogen exosphere. *Icarus*, *281*, 264–280. https://doi.org/10.1016/j.icarus.2016.08.034

Bhattacharyya, D., Clarke, J. T., Chaufray, J. Y., Mayyasi, M., Bertaux, J. L., Chaffin, M. S., et al. (2017). Seasonal changes in hydrogen escape from Mars through analysis of HST observations of the Martian exosphere near perihelion. *Journal of Geophysical Research (Space Physics)*, *122*(11), 11756–11764. https://doi.org/10.1002/2017JA024572

Bhattacharyya, D., Clarke, J. T., Mayyasi, M., Shematovich, V., Bisikalo, D., Chaufray, J. Y., et al. (2023). Evidence of non-thermal hydrogen in the exosphere of Mars resulting in enhanced water loss. *Journal of Geophysical Research (Planets)*, *128*(8), e2023JE007801. https://doi.org/10.1029/2023JE007801

Chaffin, M. S., Chaufray, J. Y., Deighan, J., Schneider, N. M., Mayyasi, M., Clarke, J. T., et al. (2018). Mars H escape rates derived from MAVEN/IUVS lyman alpha brightness measurements and their dependence on model assumptions. *Journal of Geophysical Research (Planets)*, *123*(8), 2192–2210. https://doi.org/10.1029/2018JE005574

Chaffin, M. S., Chaufray, J. Y., Deighan, J., Schneider, N. M., McClintock, W. E., Stewart, A. I. F., et al. (2015). Three-dimensional structure in the Mars H corona revealed by IUVS on MAVEN. *Geophysical Research Letters*, *42*(21), 9001–9008. https://doi.org/10.1002/2015GL065287

Chaffin, M. S., Chaufray, J.-Y., Stewart, I., Montmessin, F., Schneider, N. M., & Bertaux, J.-L. (2014). Unexpected variability of Martian hydrogen escape. *Geophysical Research Letters*, *41*(2), 314–320. https://doi.org/10.1002/2013GL058578

Chaffin, M. S., Deighan, J., Schneider, N. M., & Stewart, A. I. F. (2017). Elevated atmospheric escape of atomic hydrogen from Mars induced by high-altitude water. *Nature Geoscience*, *10*(3), 174–178. https://doi.org/10.1038/ngeo2887

Chaffin, M. S., Kass, D. M., Aoki, S., Fedorova, A. A., Deighan, J., Connour, K., et al. (2021). Martian water loss to space enhanced by regional dust storms. *Nature Astronomy*, *5*(10), 1036–1042. https://doi.org/10.1038/s41550-021-01425-w

Chaufray, J. Y., Bertaux, J. L., Leblanc, F., & Quémerais, E. (2008). Observation of the hydrogen corona with SPICAM on Mars express. *Icarus*, *195*(2), 598–613. https://doi.org/10.1016/j.icarus.2008.01.009

Chaufray, J. Y., Gonzalez-Galindo, F., Lopez-Valverde, M. A., Forget, F., Quémerais, E., Bertaux, J. L., et al. (2021). Study of the hydrogen escape rate at Mars during Martian years 28 and 29 from comparisons between SPICAM/Mars express observations and GCM-LMD simulations. *Icarus*, *353*, 113498. https://doi.org/10.1016/j.icarus.2019.113498

Chaufray, J. Y., Mayyasi, M., Chaffin, M., Deighan, J., Bhattacharyya, D., Clarke, J., et al. (2021). Estimate of the D/H ratio in the Martian upper atmosphere from the low spectral resolution mode of MAVEN/IUVS. *Journal of Geophysical Research (Planets)*, *126*(4), e06814. https://doi.org/10.1029/2020JE006814

Chirakkil, K., Deighan, J., Chaffin, M. S., Jain, S. K., Lillis, R. J., Raghuram, S., et al. (2024). EMM EMUS observations of hot oxygen corona at Mars: Radial distribution and temporal variability. *Journal of Geophysical Research (Space Physics)*, *129*(3), e2023JA032342. https://doi.org/10.1029/2023JA032342

Clarke, J. T., Bertaux, J. L., Chaufray, J. Y., Gladstone, G. R., Quemerais, E., Wilson, J. K., & Bhattacharyya, D. (2014). A rapid decrease of the hydrogen corona of Mars. *Geophysical Research Letters*, *41*(22), 8013–8020. https://doi.org/10.1002/2014GL061803

Clarke, J. T., Mayyasi, M., Bhattacharyya, D., Schneider, N. M., McClintock, W. E., Deighan, J. I., et al. (2017). Variability of D and H in the Martian upper atmosphere observed with the MAVEN IUVS echelle channel. *Journal of Geophysical Research (Space Physics)*, *122*(2), 2336–2344. https://doi.org/10.1002/2016JA023479

Deighan, J., Chaffin, M. S., Chaufray, J. Y., Stewart, A. I. F., Schneider, N. M., Jain, S. K., et al. (2015). MAVEN IUVS observation of the hot oxygen corona at Mars. *Geophysical Research Letters*, *42*(21), 9009–9014. https://doi.org/10.1002/2015GL065487

Dostovalov, S. B., & Chuvakhin, S. D. (1973). On the distribution of neutral hydrogen in the upper atmosphere of Mars. *Cosmic Research*, *11*, 687.

Eparvier, F. G., Chamberlin, P. C., Woods, T. N., & Thiemann, E. M. B. (2015). The solar extreme ultraviolet monitor for MAVEN. *Space Science Reviews*, *195*(1–4), 293–301. https://doi.org/10.1007/s11214-015-0195-2

Feldman, P. D., Steffl, A. J., Parker, J. W., A'Hearn, M. F., Bertaux, J.-L., Alan Stern, S., et al. (2011). Rosetta-alice observations of exospheric hydrogen and oxygen on Mars. *Icarus*, *214*(2), 394–399. https://doi.org/10.1016/j.icarus.2011.06.013

Feldman, P. D., Weaver, H. A., & Burgh, E. B. (2002). Far ultraviolet spectroscopic explorer observations of CO and H_2 emissions in comet C/2001 A2(Linear). *The Astrophysical Journal Letters*, *576*(1), L91–L94. https://doi.org/10.1086/343089

Forget, F., Hourdin, F., Fournier, R., Hourdin, C., Talagrand, O., Collins, M., et al. (1999). Improved general circulation models of the Martian atmosphere from the surface to above 80 km. *Journal of Geophysical Research*, *104*(E10), 24155–24176. https://doi.org/10.1029/1999JE001025

Futaana, Y., Barabash, S., Grigoriev, A., Holmström, M., Kallio, E., Brandt, P. C. s., et al. (2006). First ENA observations at Mars: ENA emissions from the Martian upper atmosphere. *Icarus*, *182*(2), 424–430. https://doi.org/10.1016/j.icarus.2005.09.019

Gunell, H., Brinkfeldt, K., Holmström, M., Brandt, P. C. s., Barabash, S., Kallio, E., et al. (2006). First ENA observations at Mars: Charge exchange ENAs produced in the magnetosheath. *Icarus*, *182*(2), 431–438. https://doi.org/10.1016/j.icarus.2005.10.027

Halekas, J. S. (2017). Seasonal variability of the hydrogen exosphere of Mars. *Journal of Geophysical Research (Planets)*, *122*(5), 901–911. https://doi.org/10.1002/2017JE005306

Halekas, J. S., Lillis, R. J., Mitchell, D. L., Cravens, T. E., Mazelle, C., Connerney, J. E. P., et al. (2015). MAVEN observations of solar wind hydrogen deposition in the atmosphere of Mars. *Geophysical Research Letters*, *42*(21), 8901–8909. https://doi.org/10.1002/2015GL064693

Halekas, J. S., Ruhunusiri, S., Harada, Y., Collinson, G., Mitchell, D. L., Mazelle, C., et al. (2017). "Structure, dynamics, and seasonal variability of the mars-solar wind interaction: Maven solar wind ion analyzer in-flight performance and science results. *Journal of Geophysical Research (Space Physics)*, *122*(1), 547–578. https://doi.org/10.1002/2016JA023167

Heavens, N. G., Kleinböhl, A., Chaffin, M. S., Halekas, J. S., Kass, D. M., Hayne, P. O., et al. (2018). Hydrogen escape from Mars enhanced by deep convection in dust storms. *Nature Astronomy*, *2*, 126–132. https://doi.org/10.1038/s41550-017-0353-4

Holsclaw, G. M., Deighan, J., Almatroushi, H., Chaffin, M., Correira, J., Evans, J. S., et al. (2021). The Emirates Mars ultraviolet spectrometer (EMUS) for the EMM mission. *Space Science Reviews*, *217*(8), 79. https://doi.org/10.1007/s11214-021-00854-3

Hunten, D. M., & McElroy, M. B. (1970). Production and escape of hydrogen on Mars. *Journal of Geophysical Research*, *75*(31), 5989–6001. https://doi.org/10.1029/JA075i031p05989

Jakosky, B. M. (2021). Atmospheric loss to space and the history of water on Mars. *Annual Review of Earth and Planetary Sciences*, *49*(1), 71–93. https://doi.org/10.1146/annurev-earth-062420-052845

Kass, D. M., Kleinböhl, A., McCleese, D. J., Schofield, J. T., & Smith, M. D. (2016). Interannual similarity in the Martian atmosphere during the dust storm season. *Geophysical Research Letters*, *43*(12), 6111–6118. https://doi.org/10.1002/2016GL068978

Krasnopolsky, V. A., & Feldman, P. D. (2002). Far ultraviolet spectrum of mars. *Icarus*, *160*(1), 86–94. https://doi.org/10.1006/icar.2002.6949

Lallement, R., Bertaux, J. L., & Dalaudier, F. (1985). Interplanetary Lyman-alpha spectral profiles and intensities for both repulsive and attractive solar force fields Predicted absorption pattern by a hydrogen cell. *A&A*, *150*(1), 21–32.

Lallement, R., Bertaux, J. L., & Kurt, V. G. (1985). Solar wind decrease at high heliographic latitudes detected from Prognoz interplanetary Lyman alpha mapping. *Journal of Geophysical Research*, *90*(A2), 1413–1424. https://doi.org/10.1029/JA090iA02p01413

Madeleine, J. B., Forget, F., Millour, E., Montabone, L., & Wolff, M. J. (2011). Revisiting the radiative impact of dust on Mars using the LMD global climate model. *Journal of Geophysical Research (Planets)*, *116*(E11), E11010. https://doi.org/10.1029/2011JE003855

Masunaga, K., Terada, N., Yoshida, N., Nakamura, Y., Kuroda, T., Yoshioka, K., et al. (2022). Alternate oscillations of Martian hydrogen and oxygen upper atmospheres during a major dust storm. *Nature Communications*, *13*(1), 6609. https://doi.org/10.1038/s41467-022-34224-6

Masunaga, K., Yoshioka, K., Chaffin, M. S., Deighan, J., Jain, S. K., Schneider, N. M., et al. (2020). Martian oxygen and hydrogen upper atmospheres responding to solar and dust storm drivers: Hisaki space telescope observations. *Journal of Geophysical Research (Planets)*, *125*(12), e06500. https://doi.org/10.1029/2020JE006500

Mayyasi, M., Bhattacharyya, D., Clarke, J., Catalano, A., Benna, M., Mahaffy, P., et al. (2018). Significant space weather impact on the escape of hydrogen from Mars. *Geophysical Research Letters*, *45*(17), 8844–8852. https://doi.org/10.1029/2018GL077727

Mayyasi, M., Clarke, J., Chaufray, J. Y., Kass, D., Bougher, S., Bhattacharyya, D., et al. (2023). Solar cycle and seasonal variability of H in the upper atmosphere of Mars. *Icarus*, *393*, 115293. https://doi.org/10.1016/j.icarus.2022.115293

McClintock, W. E., Schneider, N. M., Holsclaw, G. M., Clarke, J. T., Hoskins, A. C., Stewart, I., et al. (2015). The imaging ultraviolet spectrograph (IUVS) for the MAVEN mission. *Space Science Reviews*, *195*(1–4), 75–124. https://doi.org/10.1007/s11214-014-0098-7

McElroy, M. B. (1972). Mars: An evolving atmosphere. *Science*, *175*(4020), 443–445. https://doi.org/10.1126/science.175.4020.443

McElroy, M. B., & Donahue, T. M. (1972). Stability of the Martian atmosphere. *Science*, *177*(4053), 986–988. https://doi.org/10.1126/science.177.4053.986

McElroy, M. B., Kong, T. Y., Yung, Y. L., & Nier, A. O. (1976). Composition and structure of the Martian upper atmosphere - Analysis of results from Viking. *Science*, *194*(4271), 1295–1298. https://doi.org/10.1126/science.194.4271.1295

Meier, R. R., Anderson, J. D. E., Paxton, L. J., McCoy, R. P., & Chakrabarti, S. (1987). The OI $3d^3D^\circ$-$2p^4$ ^3P transition at 1026 Å in the day airglow. *Journal of Geophysical Research*, *92*(A8), 8767–8774. https://doi.org/10.1029/JA092iA08p08767

Millour, E., Forget, F., Spiga, A., Vals, M., Zakharov, V., Montabone, L., et al. the MCD development team (2018). The Mars climate Database (version 5.3). In (Ed.), (p. 213).

Möbius, E., Bzowski, M., Chalov, S., Fahr, H. J., Gloeckler, G., Izmodenov, V., et al. (2004). Synopsis of the interstellar He parameters from combined neutral gas, pickup ion and UV scattering observations and related consequences. *Astronomy & Astrophysics*, *426*(3), 897–907. https://doi.org/10.1051/0004-6361:20035834

Nair, H., Allen, M., Anbar, A. D., Yung, Y. L., & Clancy, R. T. (1994). A photochemical model of the Martian atmosphere. *Icarus*, *111*(1), 124–150. https://doi.org/10.1006/icar.1994.1137

Olsen, K. S., Fedorova, A. A., Trokhimovskiy, A., Montmessin, F., Lefèvre, F., Korablev, O., et al. (2022). Seasonal changes in the vertical structure of ozone in the martian lower atmosphere and its relationship to water vapor. *Journal of Geophysical Research (Planets)*, *127*(10), e2022JE007213. https://doi.org/10.1029/2022JE007213

Parkinson, T. D., & Hunten, D. M. (1972). Spectroscopy and aeronomy of O_2 on Mars. *Journal of the Atmospheric Sciences*, *29*(7), 1380–1390. https://doi.org/10.1175/1520-0469(1972)029⟨1380:SAAOOO⟩2.0.CO;2

Quémerais, E., Lallement, R., Bertaux, J. L., Koutroumpa, D., Clarke, J., Kyrölä, E., & Schmidt, W. (2006). Interplanetary Lyman α line profiles: Variations with solar activity cycle. *A&A*, *455*(3), 1135–1142. https://doi.org/10.1051/0004-6361:20065169

Rahmati, A., Larson, D. E., Cravens, T. E., Lillis, R. J., Halekas, J. S., McFadden, J. P., et al. (2018). Seasonal variability of neutral escape from Mars as derived from MAVEN pickup ion observations. *Journal of Geophysical Research (Planets)*, *123*(5), 1192–1202. https://doi.org/10.1029/2018JE005560

Slavin, J. D. (2009). The origins and physical properties of the complex of local interstellar clouds. *Space Science Reviews*, *143*(1–4), 311–322. https://doi.org/10.1007/s11214-008-9342-3

Stone, S. W., Yelle, R. V., Benna, M., Lo, D. Y., Elrod, M. K., & Mahaffy, P. R. (2020). Hydrogen escape from Mars is driven by seasonal and dust storm transport of water. *Science*, *370*(6518), 824–831. https://doi.org/10.1126/science.aba5229

Sun, M., Gu, H., Cui, J., Wu, X., Huang, X., Ni, Y., et al. (2023). Enhanced hydrogen escape on Mars during the 2018 global dust storm: Impact of horizontal wind field. *ApJ*, *953*(1), 71. https://doi.org/10.3847/1538-4357/ace43e

Thiemann, E. M. B., Chamberlin, P. C., Eparvier, F. G., Templeman, B., Woods, T. N., Bougher, S. W., & Jakosky, B. M. (2017). The MAVEN EUVM model of solar spectral irradiance variability at Mars: Algorithms and results. *Journal of Geophysical Research (Space Physics)*, *122*(3), 2748–2767. https://doi.org/10.1002/2016JA023512

Vallerga, J., Lallement, R., Lemoine, M., Dalaudier, F., & McMullin, D. (2004). EUVE observations of the helium glow: Interstellar and solar parameters. *Astronomy & Astrophysics*, *426*(3), 855–865. https://doi.org/10.1051/0004-6361:20035887

Witte, M. (2004). Kinetic parameters of interstellar neutral helium. Review of results obtained during one solar cycle with the Ulysses/GAS-instrument. *Astronomy & Astrophysics*, *426*(3), 835–844. https://doi.org/10.1051/0004-6361:20035956

Yung, Y. L., Wen, J.-S., Pinto, J. P., Allen, M., Pierce, K. K., & Paulson, S. (1988). HDO in the Martian atmosphere: Implications for the abundance of crustal water. *Icarus*, *76*(1), 146–159. https://doi.org/10.1016/0019-1035(88)90147-9

Erratum

The originally published version of this article contained a typographical error. In the last sentence of the second paragraph of Section 4, the word "perihelion" should be replaced with "aphelion." The error has been corrected, and this may be considered the authoritative version of record.